Applied Surface Science 466 (2019) 358–366

Contents lists available at ScienceDirect

Applied Surface Science

journal homepage: www.elsevier.com/locate/apsusc

Full Length Article

Studied on the graded band-gap copper indium diselenide thin film solar cells prepared by electrochemical route

Ashwini B. Rohom[a,b], Priyanka U. Londhe[a], Jeong In Han[b], Nandu B. Chaure[a,*]

[a] Electrochemical Laboratory, Department of Physics, Savitribai Phule Pune University (formerly University of Pune), Pune 411007, India
[b] Department of Chemical and Biochemical Engineering, Dongguk University-Seoul, 04620 Seoul, South Korea

ARTICLE INFO

Keywords:
$CuInSe_2$
Graded band gap
Thin film solar cells
Electrodeposition
Power conversion efficiency

ABSTRACT

A graded band-gap $CuInSe_2$ (CIS) thin film solar cell (TFSC) having glass/FTO/CdS/CIS multilayer/Au structure has been fabricated. A simple and low-cost electrodeposition technique is used to deposit the multilayers of CIS onto fluorine doped tin oxide (FTO) coated glass substrate. A conventional three-electrode geometry consisting, FTO, graphite and Ag/AgCl as a working, counter and reference electrodes, respectively was used for electrodeposition. Structural characterization was carried out using X-ray diffraction (XRD) and Raman spectroscopy, which revealed the chalcopyrite tetragonal CIS structure with a quite Cu-rich surface which reduces upon selenization. The morphology of the as grown and selenized CIS multilayer thin films was studied by using atomic force microscopy (AFM) which shows the compact and uniform layer formation. The depth profile distribution of individual elements in both as-grown and selenized CIS multilayer thin films has been determined using secondary ion mass spectroscopy (SIMS). SIMS results revealed that the proposed graded band gap structure is retained even after selenization. The presence of Cu^{+}, In^{3+} and Se^{2-} oxidation states were confirmed using X-ray photoelectron spectroscopy (XPS). A single layer and multilayer CIS solar cell devices yielded ~5.10% and ~7.20% power conversion efficiency, respectively. In the present work, pH 3 buffer solution helps to improve the morphology of CIS layer which gives the better power conversion efficiency as compared to the previously reported value.

1. Introduction

The inadequacy of fossil fuel resources, population growth and global warming facilitate to the requirements of new renewable energy sources, such as solar energy. The copper indium diselenide (CIS) based chalcopyrite solar cells are more advantageous among the all photovoltaic technologies due to the direct and tuneable band gap, large mean free path of charge carriers, high absorption coefficient and extraordinary stability [1,2]. The maximum efficiency of CIS based device has been achieved up to ~22.6% by vacuum deposition technique [3]. The vacuum based system are expensive and their day to day maintenance is high, which is increases the cost of the TFSC devices. The low-cost solution processable techniques have attracted attention owing to the low-temperature growth, less manufacturing cost and possibility to have the high throughput [4–7]. Bhattacharya et. al, reported ~15.4% efficiency of CIGS solar cell using electrodeposition method with excess Ga addition by physical vapour deposition [8].

Despite of significant economic and technical advantages, CIS based solar cells suffers relatively low-efficiency compared to the theoretical estimated efficiency ~32.21% [9]. Thus, in order to improve the performance of CIS based TFSC, it is essential to develop different strategies. Researcher now extensively focussing on the improvements of solar cells by enhancing their electrical and optical properties by harvesting shorter wavelength photons to minimize the absorption losses [10]. Several reports are available on dealing with various aspects of CIS based solar cells [11–13]. Recently the development of nanoparticles based solar cell achieves the efficiency ~12% [14]. The graded band gap structure of CIS is proposed by several groups with an enhancement in the efficiency of TFSC [15–16]. The development of a graded band gap CIS layer is reported by Chaure et al using electrodeposition technique with efficiency ~6.5% [17]. It is well known that the energy band-gap of CIS depends on the content of individual elements [18]. This property of CIS can be utilized to tailor the band gap which not only help to prevent the recombination in solar cell and help to harvest the maximum solar spectrum. The contents of individual element in the deposit can be varied by changing the growth potential. Recently, we have also reported the effect of rapid thermal annealing and normal selenization onto the CIS TFSC devices prepared by

* Corresponding author.
E-mail addresses: hanji@dongguk.edu (J.I. Han), n.chaure@physics.unipune.ac.in (N.B. Chaure).

https://doi.org/10.1016/j.apsusc.2018.10.053
Received 27 January 2018; Received in revised form 8 August 2018; Accepted 5 October 2018
Available online 06 October 2018
0169-4332/

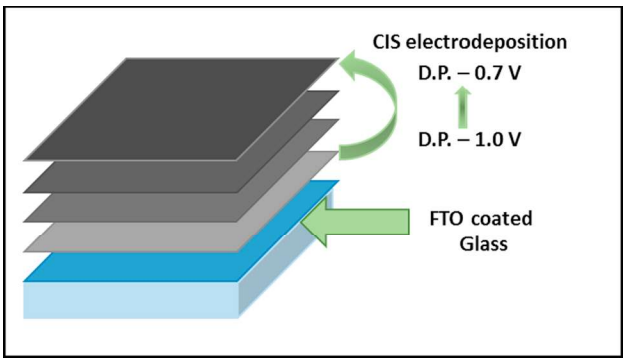

Fig. 1. Typical schematic used to grow the multilayer CIS thin films on FTO substrate using electrodeposition at various growth potentials with respect to Ag/AgCl reference electrode.

electrochemical route [19]. We have reported the effect of electrodeposition potentials on the properties on CIS layers [20].

Herein, the work on development of CIS solar cells using graded band-gap structure is described. The concept of graded band gap based CIS solar cell is demonstrated by the formation of p and n-type conducting CIS layers having different energy band gap values. This type of structure could be employed to any chalcopyrite material to get high performance for TFSC devices.

2. Experimental details

2.1. Chemicals

Copper chloride ($CuCl_2$), indium chloride ($InCl_3$), selenous acid ($H_2Se_2O_3$) and Lithium chloride (LiCl) were purchased from Sigma-Aldrich of purity at least 99.9%. Fluorine doped tin oxide (FTO) coated glass substrates of sheet resistance 10–15 Ω/□ were purchased from Pilkington glass company, UK. The double distilled deionized water (DDDW) was used as a solvent.

2.2. Electrodeposition of CIS layers

Potentiostatic electrodeposition was used to deposit CIS thin films. A convectional three-electrode assembly consisting Ag/AgCl, graphite plate and FTO coated glass substrates were used as reference, counter and working electrode, respectively. The substrates were cleaned thoroughly with DDDW in ultrasonic bath. Finally the substrates were ultrasonicated in acetone and *iso*-propanol. The electrolytes contained 2 mM $CuCl_2$, 4 mM $InCl_3$ and 3 mM $H_2Se_2O_3$ were dissolved in pH hydrion buffer (pH 3) solution. Lithium chloride (LiCl) was used as a supporting electrolyte. Cyclic voltammetry (CV) measurement was recorded to study the electrochemical behaviour of CIS system at scan rate 5 mV/sec. The electrodeposition of CIS thin films were carried out at different deposition potentials with respect to Ag/AgCl reference electrode without external agitation at room temperature. A schematic of multilayer CIS structure is depicted in Fig. 1. Immediately after deposition, the samples were rinsed in warm DDDW to remove the loosely

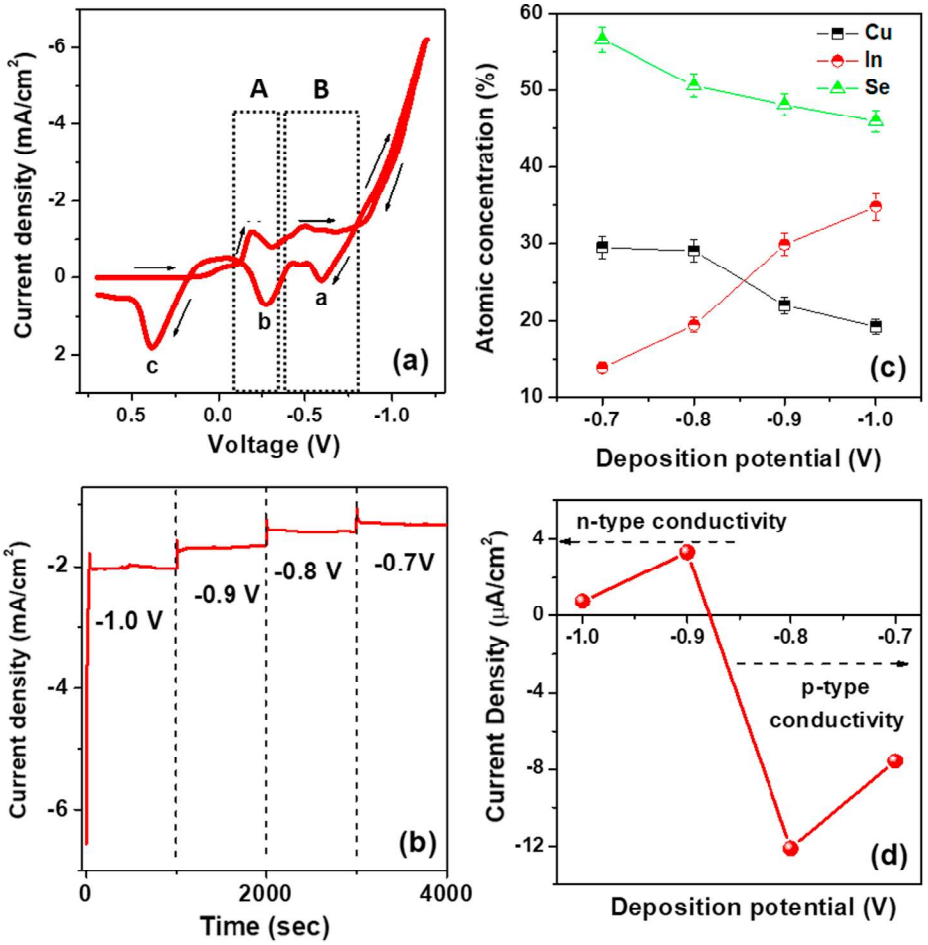

Fig. 2. (a) Cyclic voltammogram for CIS system recorded at 5 mV/sec, (b) chronoamperometric curves for multilayer CIS deposition, (c) plot for atomic concentration for elements in individual CIS layers and (d) PEC signals obtained for CIS layers grown at various deposition potentials.

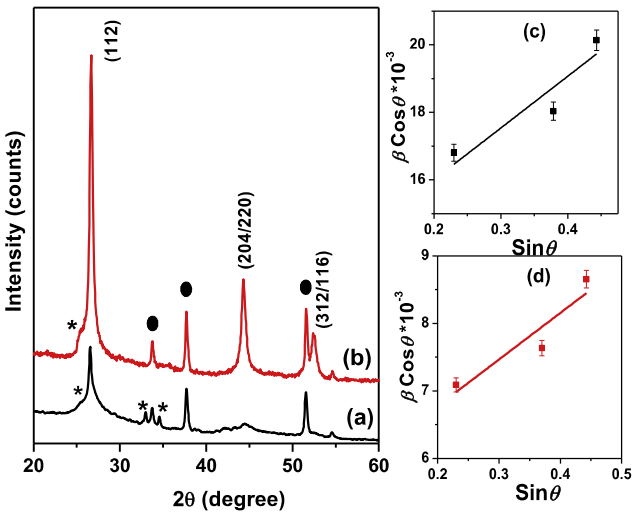

Fig. 3. XRD patterns (a, b) and plots of $\beta cos\theta$ versus sinθ (c, d) for as-deposited and selenized multilayer CIS thin films, respectively.

Table 1
A summary of the crystallite size and strain calculated from Debye Scherrer formula and Williamson-Hall analysis.

Multilayer CIS thin film	Average crystallite size from Debye Scherrer formula	Williamson-Hall analysis		
		Average crystallite size (nm)	Types of strain (Tensile 'T' or Compressive 'C')	Strain, ε ($\times 10^{-3}$)
As-deposited	8.5 nm	9.7	T	5.4
Selenized	19 nm	24	T	14.1

bound particles deposited on the surface of the sample. Subsequently, the films were dried in laboratory atmosphere over night prior to post-deposition heat treatment. The annealing process of the sample was completed in two stages with Se-ambient. Se ingots were used to make Se-ambient. Prior to make the Se-ambient the system was evacuated with Argon several times. Initially, the temperature of the furnace was maintained at 200 °C for 5 sec and subsequently raised to 450 °C within 5 sec and hold for 10 sec. Immediately, the temperature (450 °C) was reduced to 200 °C within 5 sec and hold for 5 sec. Such 10 cycles were applied and finally the samples were cooled down to room temperature with 30° per sec.

2.3. Materials characterization

Cyclic voltammetry (CV) and Chronoamperometric measurements were carried out using μ3AUT 70762 AUTOLAB potentiostat/galvanostat. The structural properties were studied by means of X-ray diffractometer, model Bruker D8 with Cu Kα anode of wavelength 0.154 nm. Optical absorption measurements were performed with UV–vis-NIR spectrometer, model JASCO V-770. Surface morphology of CIS layers were characterized by using atomic force microscopy (AFM), a JEOL JSPM-5200 scanning probe microscope using a silicon nitride cantilever. JSM 6360 A scanning electron microscope with an operating voltage 20 kV was to study the surface morphology. The elemental atomic percentage concentration was determined by energy dispersive X-ray analysis (EDAX) technique. The Potentiostat, SP 300, Biologic equipped with two probe measurement setup was employed to study the electrical (*J-V and C-V*) properties. Raman analysis was performed by Invia Renishaw micro Raman spectrophotometer, with 785 nm excitation laser. The elemental chemical states were analysed using X-ray Photoelectron Spectroscopy (XPS) K-α (Thermo Scientific Inc., UK)

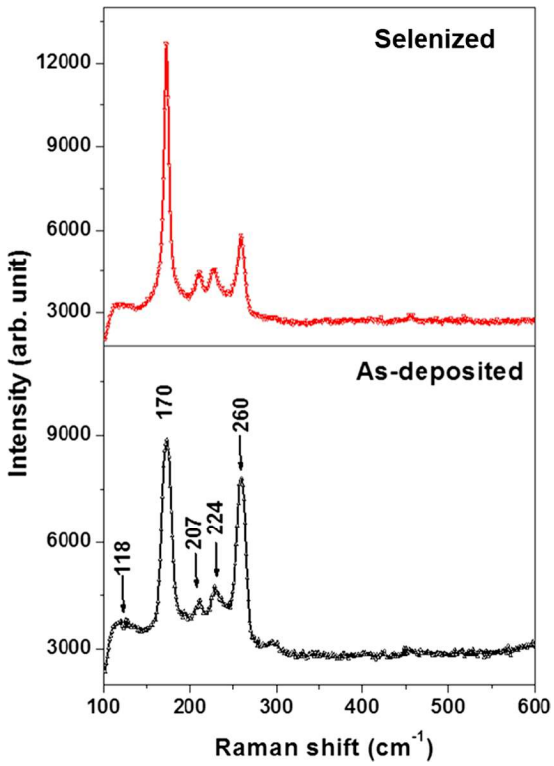

Fig. 4. Raman spectra for as-deposited (a) and selenized (b) multilayer CIS thin films.

equipped with a monochromatic X-ray source, Al Kα of energy 1486.6 eV with double focusing hemispherical analyser.

2.4. Fabrication of solar cells

The standard superstrate solar cell configuration consists, Glass/FTO/CdS/multilayer CIS/Au contact and glass/FTO/CdS/CIS/Au contact were prepared. CIS layer in single layer solar cell was deposited at –0.8 V with respect to Ag/AgCl. CdS layer of thickness ~50 to 70 nm was prepared by chemical bath deposition and annealed in air at 450 °C pior to the CIS depostion [21]. The selenized CIS sample were etched in bromine methanol solution for 60 sec to remove the unwanted secondary phases formed during the rapid thermal annealing process. The circular Au-metal contacts of diameter 3 mm were evaporated using the homemade thermal evaporation at vacuum ~5×10^{-5} torr. The final solar cell devices were measured under dark and upon illumination with Air Mass (AM) 1.5 (100 mW/cm^2).

3. Results and discussion

Four different deposition potentials, −0.7 V to −1.0 V were selected to grow the CIS multilayers (Fig. 1). In our earlier report, we have demonstrated that the CIS layers grown at −0.7 V and −0.8 V were Cu-rich with p-type conductivity and the layers grown at −0.9 V and −1 V were n-type due to growth of In-rich CIS thin films [20]. The structure proposed in Fig. 1 is multi-junction solar cell and could be useful to harvest the maximum solar spectrum with reduction in recombination losses. Fig. 2 a) depicts the cyclic voltammogram for CIS in pH 3 buffer solution. The features observed in the region 'A' (−0.1 V to −0.35 V) are assigned to reduction of Cu^{2+} and Se^{2-} ions [22]. Further, the reduction of In^{3+} along with Cu^{2+} and Se^{2-} is proposed in region 'B' (−0.35 V to −1.0 V). The detail reaction mechanism in discussed in our earlier publication (7). The sharp rise in the current beyond −1 V is associated to the deposition of In-rich CIS thin films [23]. The plateau region observed from −0.7 V to −1.0 V offers the

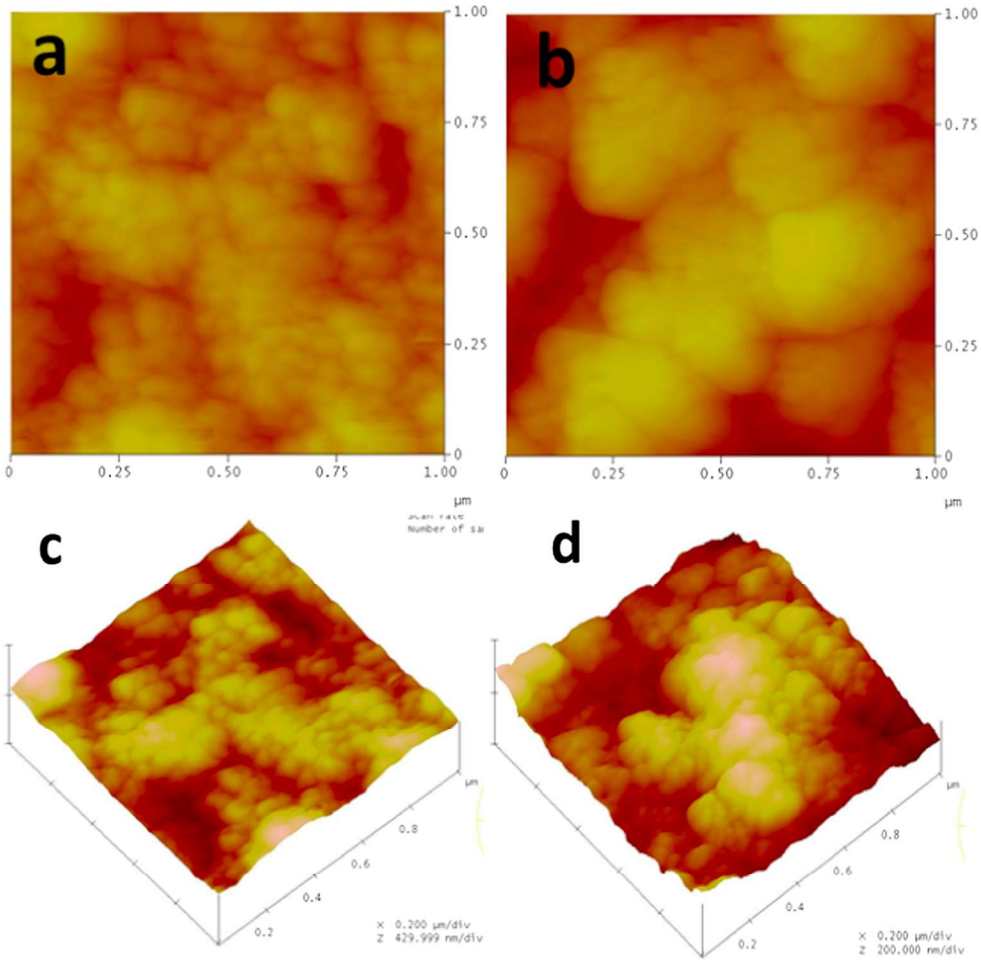

Fig. 5. 2-dimesional and 3-dimensional AFM images for as-deposited (a, c) and for selenized (b, d) multilayer CIS thin films.

suitable deposition potentials for CIS. During the reverse (anodic) scan the peaks related to stripping of In-rich, Cu-rich and Se-rich CIS are clearly seen which marked as 'a', 'b' and 'c', respectively. Fig. 2 b) shows the Chronoamperometric curve for CIS multilayer deposited at various deposition potential to obtain the graded band gap structure. The increased current upon increasing the growth potential is associated to the more mass transport towards the cathode (working electrode). The compositional studies on CIS layers electrodeposited at various deposition potentials were performed using Energy dispersive spectroscopy (EDS). Fig. 2 c) shows the atomic percentage concentration of Cu, In and Se determined by EDS analysis for the sample grown at various deposition potentials [20]. It can be clearly seen that with increasing the deposition potential the Cu contents in the layers decreases, while the In contents increases, respectively. The content of the selenium was measured nearly consists ~50% for the layer grown at different deposition potential. The conductivity type of the CIS layer was studied using the photo-electrochemical cell measured. The photocurrent measured for the samples grown at different deposition potentials is given in Fig. 2d). It is confirmed that the lower cathodic potential leads to grow p-type and higher potential supports to deposit n-type conductivity CIS layers. The results of individual CIS layers grown at various deposition potentials are already discussed in our previous report [20].

Fig. 3 a) and b) shows the XRD pattern for as-deposited and selenized multilayer CIS thin films. Three diffraction peaks attributed at 26.57°, 44.32° and 52.25° are indexed to the crystal planes (112), (204/220) and (312/116) of chalcopyrite CIS (JCPDS card No. 35-1349). Peaks related to FTO substrate are marked as solid circles (•). Binary phases of Cu_XSe_Y related peaks (marked as *) are also observed in as-prepared CIS multilayers. It is noteworthy that the reflection associated to Cu_XSe_Y are substantially minimized (nearly negligible) upon selenization. The presence of Cu_XSe_Y related peaks in XRD pattern is obvious since the top surface layer is deposited at -0.7 V which deposits Cu-rich CIS layer, which may be removed with proper surface treatment procedure. Highly polycrystalline CIS multilayer thin film was obtained upon the selenization. We further used Williamsons-Hall (W-H) relation [24] to estimate the values of average crystallite size and strain;

$$\beta \cos\theta = \varepsilon \sin\theta + \frac{\lambda}{t} \quad (1)$$

where, 'β' is the FWHM of diffraction peaks, 'θ' is the Bragg diffraction angle, 'λ' is the wavelength of X-ray source 'ε' is the strain and 't' is the average crystallite size. The values of the strain are calculated from the slope of plot of $\beta\cos\theta$ versus sinθ, whereas the inverse of intercept gives the average crystallite size. Fig. 3 c) and d) depicts the plot of $\beta\cos\theta$ versus sinθ for as-deposited and selenized multilayer CIS thin films, respectively. The values of strain for as-deposited and annealed samples were estimated $\sim 5.4 \times 10^{-3}$ and 14.1×10^{-3}, respectively. The increase in strain upon selenization could be associated to the enhancement in the crystallite size as well as recrystallization of CIS layer [25]. The values of the average crystallite size ~9.7 and 24 nm were calculated for as-deposited and selenized multilayer CIS thin films, respectively. The values of average crystallite size were further computed from the classical Debye Scherrer relation, which are in good agreement with the values calculated from W-H equation. The values of crystallite size and strain calculated from Debye Scherrer formula and Williamson-

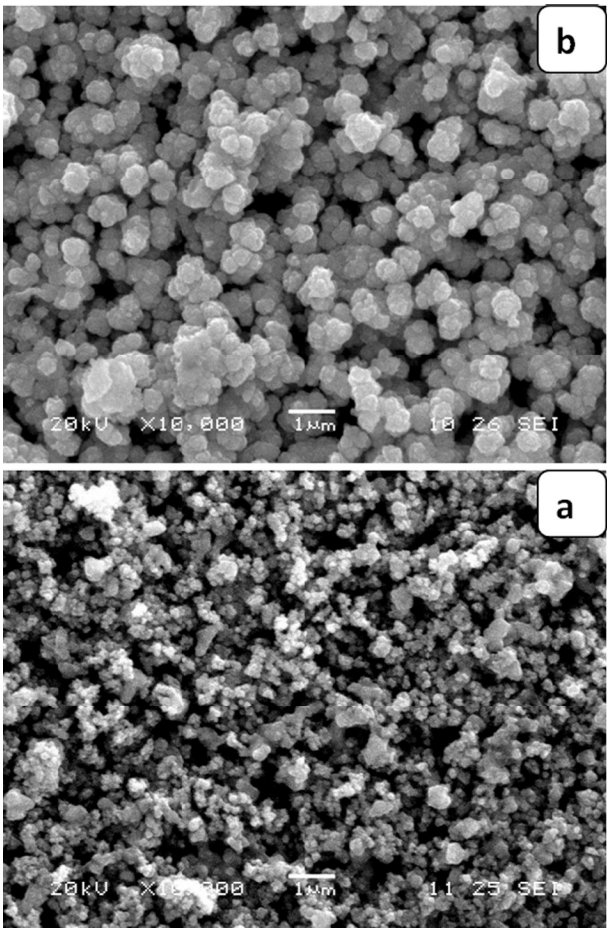

Fig. 6. SEM micrographs for a) as-deposited and b) selenized multilayer CIS thin films.

Hall analysis are summarized in Table 1.

Raman spectra for as-deposited and selenized multilayer CIS thin films are shown in Fig. 4. The presence of three peaks at 170 cm^{-1}, 207 cm^{-1} and 224 cm^{-1} confirms the ternary CIS phase formation. The most intense peak observed at 170 cm^{-1} is attributed to the characteristics A1 mode of the chalcopyrite CIS phase. The peak at 207 cm^{-1} and 224 cm^{-1} shows the presence of first contribution of E and B2 modes of CIS phase [26]. In the as-deposited spectra, the strong mode appeared at 260 cm^{-1} whose intensity decreases after selenization, could be associated to Cu_XSe_Y secondary phase [27]. The presence of peak related binary phases of Cu_XSe_Y is due to the Cu-rich surface, which agrees with the XRD result. The peak appeared at 118 cm^{-1} belongs to the laser line which was used for the calibration of the Raman wave number.

Fig. 5 depicts the 2-dimesional (2-D) and 3-dimesional (3-D) AFM micrographs for as-deposited and selenized multilayer CIS thin films. The 2-D AFM image confirms the granular morphology for the as-deposited CIS layers having particle size ~100 nm. Upon selenization agglomeration of particle takes place and the large clusters are observed. The 3-D AFM image confirms that the surface roughness increases upon selenization which is associated to the improvement in the particle size. The large area of the samples was investigated with scanning electron microscopy (SEM). Fig. 6 a) and b) shows the SEM micrographs of as-deposited and selenized multilayer CIS samples, respectively. The layers were found to be deposited all over the substrate uniformly. The particle size, ~100 nm and loosely bound particles with agglomeration of tiny particles can be seen in as-deposited sample. The dark spots observed in SEM images are due to the over growth of particles and this area was not in the focus. Densely packed, uniform,

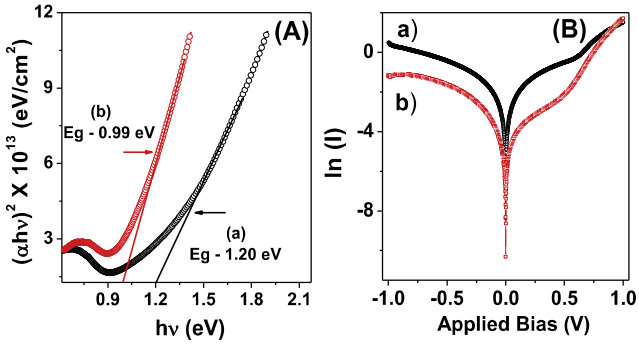

Fig. 7. (A) $(\alpha h\upsilon)^2$ versus hυ plot and (B) semi logarithmic graphs of ln(I) verses applied bias for as-deposited (a) and selenized (b) multilayer CIS thin films.

cauliflower like particles of size ~0.5–1 μm were grown upon selenization. Further the physical appearance of the sample was changed from blackish to grayish black. The formation of large particles upon selenization is proposed due to the re-crystallization of the surface of sample.

Fig. 7 A) shows the $(\alpha h\upsilon)^2$ versus $h\upsilon$ plots for as-grown and selenized CIS layers. The values of the energy band-gap 1.20 and 0.99 eV, were estimated by extrapolating the straight line portion to x-axis for as-deposited and annealed CIS multilayer thin films, respectively [28]. The band gap decreases upon selenization is proposed due to the re-crystallization of layers as well as the formation of large sized clusters. The electrical current-voltage measurements were performed to obtain the various diode parameters. Fig. 7 B) depicts the semilogarithmic plots of ln (I) versus applied bias for as-grown and selenized multilayer CIS thin films.

The value of the ideality factor (n) is calculated from the slope of linear region of the forward bias by using the following relation [29],

$$n = \frac{q}{kT}\frac{dV}{d(\ln I)} \quad (2)$$

where 'q', V, n, k, T and I are the charge of electron, applied voltage, ideality factor, Boltzmann constant, temperature and diode current, respectively. The values of ideality factor are found to be 1.40 and 1.13 for as-grown and selenized multilayer CIS thin films, respectively. The decrease in the ideality factor value after selenization can be attributed to decrease in grain boundaries of CIS thin films upon annealing as well as the growth of highly semiconducting layer.

To investigate the chemical state and composition, XPS study were carried out. Fig. 8 shows the XPS survey spectrum for as-deposited and

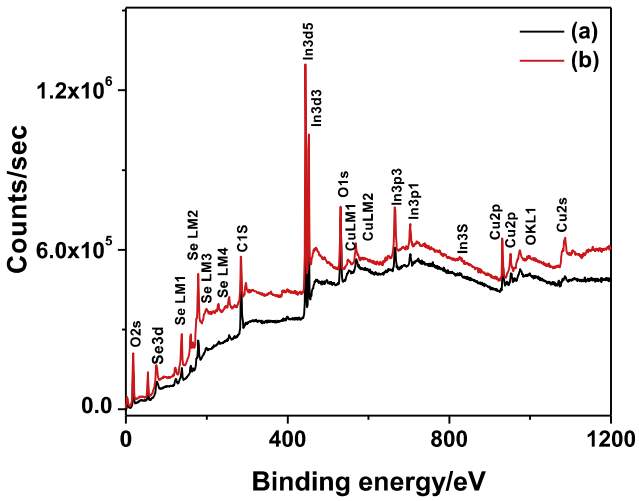

Fig. 8. XPS survey scan for as-deposited (a) and selenized (b) multilayer CIS thin films grown on FTO substrate.

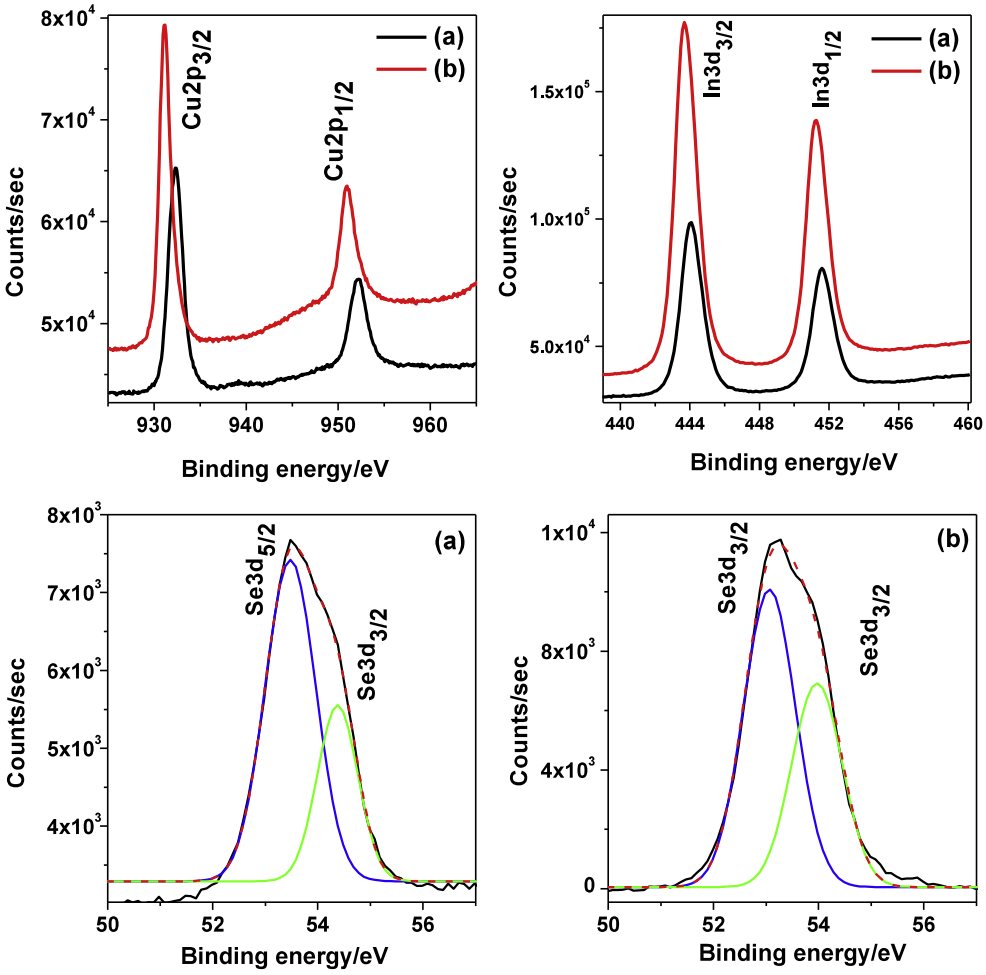

Fig. 9. Core level XPS spectra for Cu, In and Se in as-deposited (a) and selenized (b) multilayer CIS thin films.

selenized CIS multilayers, which reveals the presence of copper, indium, selenium, oxygen and carbon. No impurity related elements were detected in the XPS spectrum. Appropriate electrical charge compensation was employed to perform the analysis. Core level XPS spectra for copper, indium and selenium were examined and depicted in Fig. 9. The Cu 2p core level split into $2p_{3/2}$ (931.74 eV) and $2p_{1/2}$ (952.45 eV) peaks exhibited the Cu valence state in CIS is +1. Similarly, core level spectrum of In 3d split into two peaks $3d_{5/2}$ (443.98 eV) and $3d_{1/2}$ (451.96 eV) demonstrated the valence state of In in CIS to be +3. The Core level XPS spectra for Se3d are deconvoluted into two peaks located at 54.17 and 54.60 eV corresponding to $Se3d_{5/2}$ and $Se3d_{3/2}$ levels [30]. This confirms the presence of Cu, In and Se in Cu^{+}, In^{3+} and Se^{2-} electronic states. Moreover, all peaks shifted towards lower binding energies after selenization, which could be due to the difference

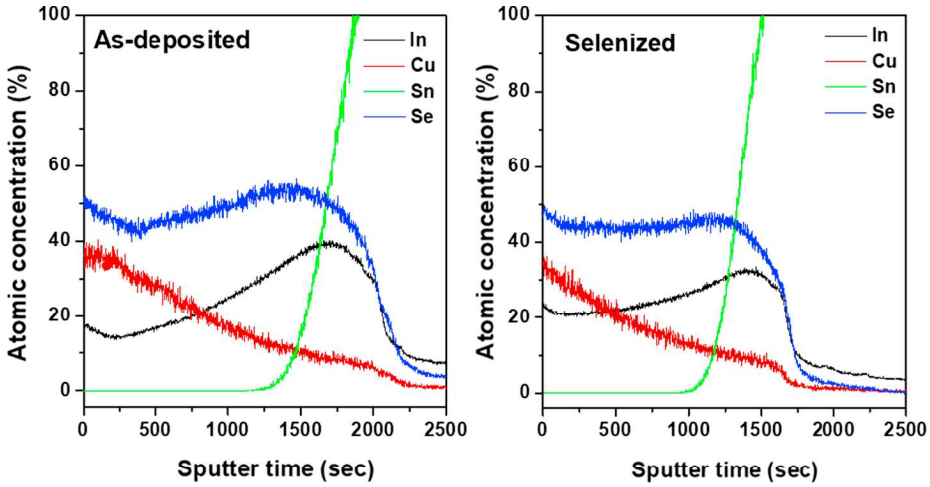

Fig. 10. SIMS depth profile for multilayer CIS thin films electrodeposited on FTO substrate. Cu, In, Ga and Se are measured in atom percentage. Sn shown for reference only as substrate.

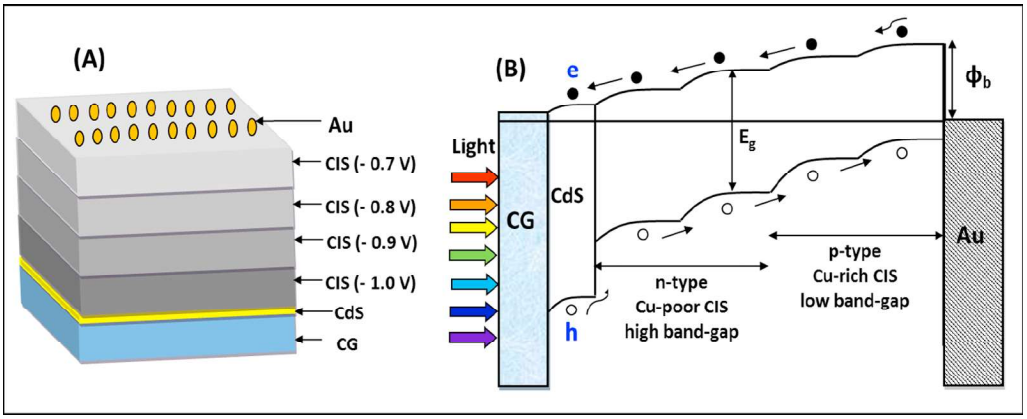

Fig. 11. (A) Schematic for multilayer structure used for CIS solar cell and (B) proposed energy-band diagram for CIS solar cell based on PEC analysis.

between the oxidation states of Cu, In and Se present in the CIS layers [31].

Fig. 10 shows the secondary ion mass spectrometry (SIMS) elemental depth profiles for Cu, In, Se, and Sn measured with the use of calibrated sample to quantify the concentration of elements in the as-deposited and selenized CIS layers. The SIMS analyses of both sample illustrates the Cu-rich surface, which goes well with the deposition of Cu-rich CIS at lower cathodic potentials. However, the contents of the Cu are found to be reduced close to the substrate because the first layer was grown at higher cathodic potential (−1.0 V), which produce Cu deficient CIS layers. For indium the behaviour is opposite, at surface the layer is In-rich, while near to substrate the contents of In were maximum. The behaviour of copper and indium in the multilayer CIS thin films is associated to the proposed structure of multilayer (Fig. 1). It was confirmed that the structure of multilayer retains upon selenization. The results obtained from EDS are consistent with the trends observed in SIMS analysis for elements in CIS layers demonstrates that the proposed structure is well formed and could be applicable to develop the multilayer solar cell in order to improve the light absorption and hence efficiency due to the graded band gap structure.

Fig. 11 A) shows the schematic diagram to fabricate the multilayer thin film solar cells FTO/CdS/multilayer-CIS/Au). Based on the absorption, PEC and EDS results discussed earlier the proposed energy band diagram of multilayer CIS thin film solar cell is represented in

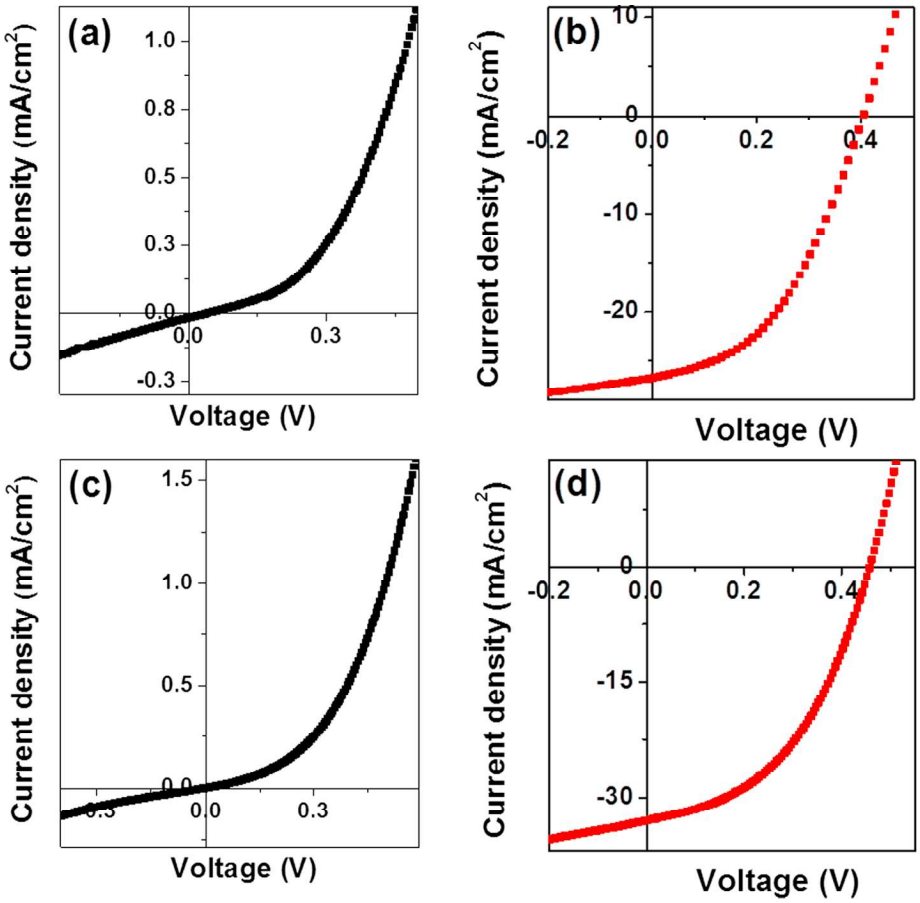

Fig. 12. The dark and illuminated J-V characteristics measured for glass/FTO/CdS/single layer CIS/Au (a) and (b) and glass/FTO/CdS/multilayer CIS/Au (c) and (d), respectively.

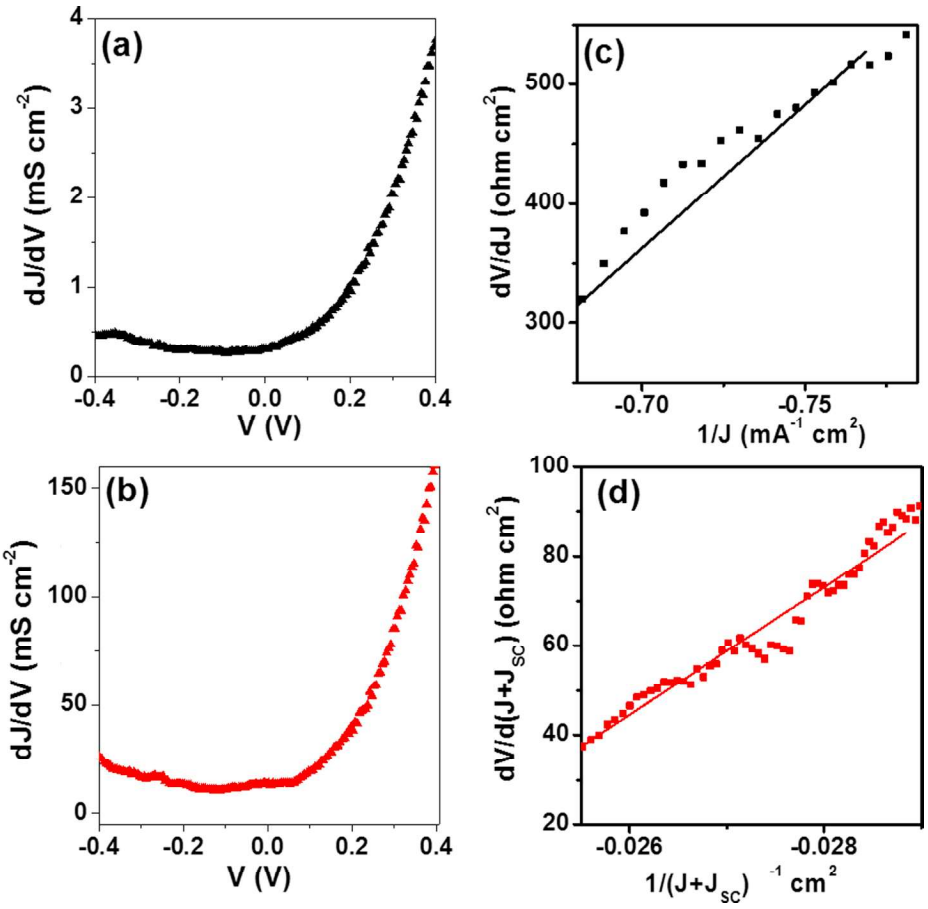

Fig. 13. Plot for dJ/dV versus V (a, b) and corresponding plot for of dV/dJ versus 1/(J) (c) and dV/d(J + J_{SC}) versus 1/(J + J_{SC}) (d) illustrated from J-V characteristics for superstrate configuration of heterostructure consisting glass/FTO/CdS/multilayer CIS/Au under dark and illuminated conditions, respectively.

Table 2
Solar cell parameters obtained from single layer and multilayer CIS thin film solar cell under dark and illuminated conditions.

Cell	V_{OC} (mV)	J_{SC} (mA/cm^2)	FF	η %	G (dark) (mS/cm^2)	G (I) (mS/cm^2)	R_S (dark) Ω cm^2	R_S (I) Ω cm^2
Glass/FTO/CdS/Single layer CIS/ Au-contact	405	26	48	5.10	0.51	38.12	350.2	40.0
Glass/FTO/CdS/Multilayer CIS/ Au-contact	460	32	49	7.20	0.47	26.22	314.4	37.4

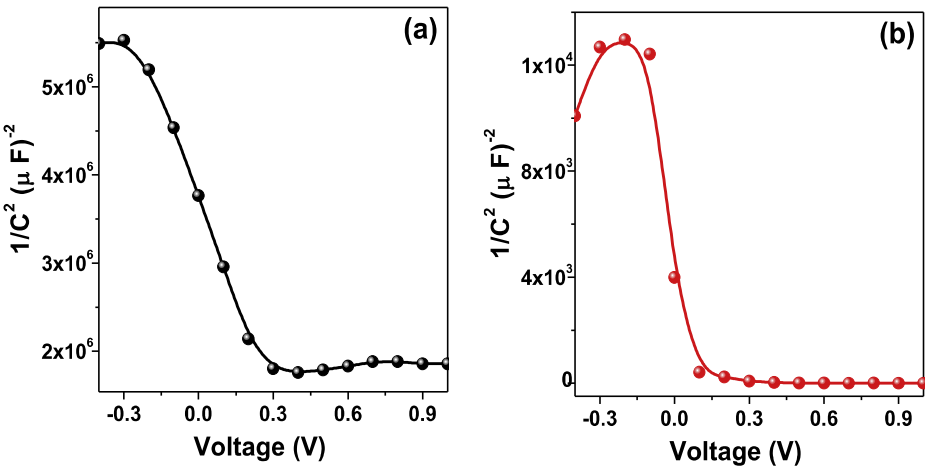

Fig. 14. Mott-Schottky plots for multilayer CIS solar cell under dark (a) and illuminated (b) conditions.

Fig. 11 B). The proposed band diagram assumes the absence of any cliff type structure at the interfaces. The maximum photons should be absorbed and the recombination losses can be reduced by depositing the multilayers of CIS of different band energy and conductivity type.

The dark and illuminated J-V characteristics of a single layer and multilayer CIS solar cell are given in Fig. 12 a), c) and b), d), respectively. Note a single layer structure of CIS solar cell was prepared at growth potential −0.8 V. The CIS layers obtained at −0.8 V were nearly stoichiometric and without secondary phases. Under illumination (100 mW/cm^2), a single layer and multilayer CIS solar cell structure measured 5.10% and 7.20% power conversion efficiency. The fill factor and V_{oc} measured for both solar cell structures were nearly similar. However, the remarkable enhancement noticed in the J_{sc} for multilayer structure, which could be associated to the absorption of more photons with different energies and decrease the recombination of electron hole due to the multilayer graded band gap structure.

The series resistance and shunt conductance of cell was calculated by the general diode equation [32],

$$J = J_0 exp\left[\frac{q}{nkT}(V - R_S J)\right] + GV - J_L \quad (3)$$

where, J and V are the diode current density and applied bias voltage, J_0 is the reverse saturation current density, J_L is the photocurrent density, R_s is the series resistance and G is the shunt conductance.

Fig. 13 (a-d) shows the plots of dJ/dV versus V and dV/dJ versus $(J + J_{sc})^{-1}$ derived from the dark and illuminated I-V characterization. The values of series resistance (R_S) is high ~37 Ω cm^2, which reduced further to improve the PCE. The calculated values of shunt conductance (G) and R_S for single layer (curves not shown here) and multilayer CIS cells are summarized in Table 2.

The flat band potential and carrier concentration was determined by Mott-Schottky (M-S) plot. The M-S ($1/C^2$) versus applied bias, V) plot for multilayer CIS solar cell measured under dark and illuminated conditions for frequency 100 Hz are shown in Fig. 14. Three distinct regions namely inversion, depletion and accumulation are seen in M-S plots. The following expression was used to calculate the carrier concentration by using the expression [33],

$$1/C^2 = \frac{2}{q\varepsilon_s A^2 N}(V_{bi} - V) \quad (4)$$

where, V_{bi} is the flat band potential and N is the charge carrier concentration.

The flat band potential can be determined by extrapolating the linear portion to x-axis. The values of carrier concentrations and flat band potential for CIS solar cell in dark and illuminated condition were estimated to be 1.62×10^{16} cm^3, 0.28 V and 1.25×10^{18}, 0.11 V, respectively. The value of capacitance under illumination was increased due to the trapping of photo-generated charge carriers at the defects states within the band gap.

4. Conclusion

In summary, the low-cost electrodeposition technique can be used to control the band energy and conductivity of the ternary CIS layer. XRD and Raman studies revealed the Cu-rich CIS multilayers with tetragonal crystal structure. The surface of selenized CIS multilayer was smooth, uniform and compact with spherical morphology. The energy band-gap values 1.20 eV and 0.99 eV were estimated and selenized CIS multilayer. SIMS analysis revealed the formation of proposed graded band gap structure. XPS confirmed the presence of Cu, In and Se in +1, +3 and −2 oxidation states in CIS thin films. The estimated values of carrier concentration using M-S plot are 1.62×10^{16} cm^3 and 1.25×10^{18} measured under dark and illuminated condition. A single layer and multilayer CIS solar cell devices measured ~5.10% and ~7.20% power conversion efficiency, respectively. The calculated values of series resistance are large which need to reduced further to improve the PCE. The results demonstrate that the proposed multilayer graded band gap structure could be applicable for the development of various chalcopyrite materials.

Acknowledgment

This research was supported by India-Korea Research Internship (IKRI) Program through the National Research Foundation (NRF), Korea and Department of Science Technology (DST), India and by Basic Science Research Program through the NRF funded by the Ministry of Education (NRF-2017R1D1A1B03030456). The financial support received from DST (SERI, DST/TM/SERI/FR/124(G)) is gratefully acknowledged.

References

[1] A.N. Tiwari, D.K. Pandya, K.L. Chopra, Solar Cells 22 (1987) 263–273.
[2] I. Khatri, H. Fukai, H. Yamaguchi, M. Sugiyama, T. Nakada, Sol. Energy Mater. Sol. Cells 155 (2016) 280–287.
[3] M.A. Green, K. Emery, Y. Hishikawa, W. Warta, E.D. Dunlop, Prog. Photovolt. Res. Appl. 24 (2016) 905–913.
[4] A.R. Uhl, J.K. Katahara, H.W. Hillhouse, Energy Environ. Sci. 9 (2016) 130–134.
[5] P.U. Londhe, A.B. Rohom, N.B. Chaure, RSC Adv. 5 (2015) 89635–89643.
[6] H.S. Jadhava, R.S. Kalubarmea, S. Ahnb, J.H. Yunb, C. Parka, Applied Surface Science 268 (2013) 391–396.
[7] A.B. Rohom, P.U. Londhe, N.B. Chaure, J. Solid State Electrochem. 19 (2014) 201–210.
[8] R.N. Bhattacharya, J.F. Hiltner, W. Batchelor, M.A. Contreras, R.N. Noufi, J.R. Sites, Thin solid Films 361–362 (2000) 396–399.
[9] W. Schckley, H. Queisser, J. Appl. Phys. 32 (1961) 510–519.
[10] I.M. Dharmadasa, A.A. Ojo, H. Salim, R. Dharmadasa, Energies 8 (2015) 5440–5448.
[11] T.W. Chang, Y.H. Su, W.H. Lee, 14. J. Electrochem. Soc. 161 (2014) E167–172.
[12] T. Wu, F. Hu, J. Huang, C. Chang, C. Lai, Y. Yen, H. Huang, H. Hong, A. Wang, A. Shen, J. Shieh, ACS Appl. Mater. Interfaces 6 (2014) 4842–4849.
[13] J.H. Park, I.S. Yang, Micro-Raman spectroscopy in polycrystalline $CuInSe_2$ formation, Appl. Phys. A 58 (1994) 125–128.
[14] S.M. Mcleaod, J.C. Hages, N.J. Carter, R. Agrawal, Prog. Photovolt. Res. Appl. 23 (2015) 1550–1556.
[15] N.B. Chaure, A.P. Samantillleke, R.P. Burton, J. Young, I.M. Dharmadasa, Thin Solid Films 472 (2005) 212–216.
[16] A.A. Ojo, I.M. Dharmadasa, Solar Energy 136 (2016) 10–14.
[17] N.B. Chaure, J. Young, A.P. Samantilleke, I.M. Dharmadasa, Sol. Energy Mater. Solar Cells 81 (2004) 125–133.
[18] N. Kavcar, M.J. Carter, R. Hill, R. Sol, Energy Mat. Solar Cells 27 (1992) 13–23.
[19] A.B. Rohom, P.U. Londhe, N.B. Chaure, J. Elctrochem. Soc. 165 (2018) H3051–H3060.
[20] A.B. Rohom, P.U. Londhe, G.R. Bhand, M.G. Lakhe, N.B. Chaure, J Mater Sci: Mater Electron 27 (2016) 12374–12384.
[21] N.B. Chaure, S. Bordas, A.P. Samantilleke, S.N. Chaure, J. Haigh, I.M. Dharmadasa, Thin Solid Films 437 (2003) 10–17.
[22] R.N. Bhattacharya, M. Oh, Y. Kim, Sol. Energy Mat. Solar Cells 98 (2012) 198–202.
[23] A.B. Rohom, P.U. Londhe, N.B. Chaure, Thin Solid Films 642 (2017) 303–310.
[24] B.D. Cullity, S.R. Stock, Elements of x-ray diffraction, NJ Prentice-Hall Inc., Englewood Cliff, 2001.
[25] S. Nawale, V. Ravi, I.S. Mulla, Sens. Actuat., B 139 (2009) 466–1170.
[26] A. Chao, S. Ahn, J.H. Yun, J.G. Wak, S.K. Ahn, K. Shin, H. Song, K.H. Yoon, Sol. Energy Mater. Sol. Cells 109 (2003) 17–25.
[27] J.H. Park, I.S. Yang, Appl. Phys. A 58 (1994) 125–128.
[28] C.C. Thompson, Ultraviolet-visible absorption spectroscopy, Willard Grant Press, 2007.
[29] S.M. Sze, K.K. Ng, Physics of Semiconductor Devices, IIIrd edn., Wiley, New York), 2007, pp. 170–171.
[30] J. Han, C. Liao, L. Cha, T. Jiang, H. Xie, K. Zhao, M.P. Besland, J. Phys. Chem. Solids 75 (2004) 1279–1283.
[31] B. Canava, J. Vigneron, A. Etcheberry, J.F. Guillemoles, D. Lincot, Appl. Surf. Sci. 202 (2002) 8–14.
[32] S.S. Hegedus, W.N. Shafarman, Thin-film solar cells device measurements and analysis, Prog. Photovolt. Res. Appl. 12 (2004) 155–176.
[33] S. Hamrouni, M.F. Boujmil, K. Ben Saad, Electrical properties of the Al/$CuInSe_2$ thin film Schottky junction, advances in materials, Phys. Chem. 4 (2014) 224–235.